HHS Public Access

Author manuscript

J Magn Reson Imaging. Author manuscript; available in PMC 2022 February 01.

Published in final edited form as:

J Magn Reson Imaging. 2021 February ; 53(2): 628–639. doi:10.1002/jmri.27393.

Improved characterization of diffusion in normal and cancerous prostate tissue through optimization of multicompartmental signal models

Christopher C Conlin, PhD[1], **Christine H Feng, MD**[2], **Ana E Rodriguez-Soto, PhD**[1], **Roshan A Karunamuni, PhD**[2], **Joshua M Kuperman, PhD**[1], **Dominic Holland, PhD**[3], **Rebecca Rakow-Penner, MD, PhD**[1], **Michael E Hahn, MD, PhD**[1], **Tyler M Seibert, MD, PhD**[1,2,4], **Anders M Dale, PhD**[1,3,5]

[1]Department of Radiology, UC San Diego School of Medicine, La Jolla, CA, USA

[2]Department of Radiation Medicine and Applied Sciences, UC San Diego School of Medicine, La Jolla, CA, USA

[3]Department of Neurosciences, UC San Diego School of Medicine, La Jolla, CA, USA

[4]Department of Bioengineering, UC San Diego Jacobs School of Engineering, La Jolla, CA, USA

[5]Halıcıoğlu Data Science Institute, UC San Diego, La Jolla, CA, USA

Abstract

Background: Multicompartmental modeling outperforms conventional DWI in the assessment of prostate cancer. Optimized multicompartmental models could further improve the detection and characterization of prostate cancer.

Purpose: To optimize multicompartmental signal models and apply them to study diffusion in normal and cancerous prostate tissue *in vivo*.

Study Type: Retrospective.

Subjects: 46 patients who underwent MRI examination for suspected prostate cancer; 23 had prostate cancer and 23 had no detectable cancer.

Field strength/Sequence: 3T multi-shell diffusion-weighted sequence.

Assessment: Multicompartmental models with 2–5 tissue compartments were fit to DWI data from the prostate to determine optimal compartmental ADCs. These ADCs were used to compute signal contributions from the different compartments. The Bayesian Information Criterion (BIC) and model-fitting residuals were calculated to quantify model complexity and goodness-of-fit. Tumor contrast-to-noise ratio (CNR) and tumor-to-background signal intensity ratio (SIR) were computed for conventional DWI and multicompartmental signal-contribution maps.

Statistical Tests: ANOVA and two-sample t-tests (α=0.05) were used to compare fitting residuals between prostate regions and between multicompartmental models. T-tests (α=0.05)

Corresponding Author: Anders M Dale, Address: Altman Clinical and Translational Research Institute, 9452 Medical Center Drive, 4W 228, La Jolla, CA 92037, Telephone: (858) 822-6671, andersmdale@gmail.com.

were also used to assess differences in compartmental signal-fraction between tissue types and CNR/SIR between conventional DWI and multicompartmental models.

Results: The lowest BIC was observed from the 4-compartment model, with optimal ADCs of 5.2e-4, 1.9e-3, 3.0e-3, and >3.0e-2 mm^2/s. Fitting residuals from multicompartmental models were significantly lower than from conventional ADC mapping ($P<0.05$). Residuals were lowest in the peripheral zone and highest in tumors. Tumor tissue showed the largest reduction in fitting residual by increasing model order. Tumors had a greater proportion of signal from compartment 1 than normal tissue ($P<0.05$). Tumor CNR and SIR were greater on compartment-1 signal maps than conventional DWI ($P<0.05$) and increased with model order.

Data Conclusion: The 4-compartment signal model best described diffusion in the prostate. Compartmental signal-contributions revealed by this model may improve assessment of prostate cancer.

Keywords

Restriction spectrum imaging; Multi-shell diffusion weighted imaging; Diffusion signal model; Prostate cancer

Introduction

While biopsy is the standard technique for diagnosing prostate cancer, it is prone to sampling errors that can significantly impact risk stratification and treatment (1, 2). Multiparametric MRI has become a useful tool for improving diagnostic capabilities, aiding in the detection and characterization of prostate tumors, as well as providing image guidance for biopsy and focal intervention (3–6). A critical component of multiparametric MRI is diffusion-weighted imaging (DWI), which measures the diffusion properties of water at a microscopic level to assess tissue microstructure (7).

On conventional DWI, cancerous lesions are characterized by decreased apparent diffusion coefficients (ADCs) compared to normal prostate tissue (3). However, the expected changes in ADC that accompany cancer are often confounded by edema or necrosis (8) and may not be detectable from ADC maps alone (9). It is particularly difficult to identify cancer in the transition zone of the prostate due to the common occurrence of benign prostatic hyperplasia (BPH), which exhibits DWI signal and ADC characteristics similar to that of tumors (10, 11).

Restriction spectrum imaging (RSI) is a multicompartmental approach to DWI that employs a multi-shell diffusion acquisition and high b-values to account for cellular geometry and compartmentalization (8, 12, 13). RSI and other multicompartmental DWI methods (14, 15) model the diffusion-weighted signal as a linear combination of exponential decays, with the individual decay-curves corresponding to different tissue compartments. The ADC value of each compartment is fixed, and variation in diffusion signal between voxels is, therefore, interpreted as variation in the proportion of each tissue compartment comprising the total diffusion signal. Fixing compartmental ADC values enables linearization of the DWI signal decay and rapid discrimination of the different tissue compartments within each voxel (12).

Meaningful assessment of prostate cancer with RSI requires that the number of signal-model compartments and their corresponding ADC values accurately characterize the diffusion properties of both normal and cancerous prostate tissue. Previous studies demonstrated improved discrimination between normal and cancerous prostate tissue using simple 2-compartment RSI models, with fixed ADC values corresponding to restricted and free diffusion of water (16–19) but stopped short of determining optimal ADC values or comparing it to higher-order models with additional tissue compartments. Optimizing the number of tissue compartments and associated ADCs of the RSI signal model could lead to improved characterization of prostate cancer and better discrimination of tumors in radiographically-complex regions like the transition zone.

This study aimed to optimize multicompartmental RSI models and apply them to study the diffusion properties of normal and cancerous prostate tissue *in vivo*.

Materials and Methods

This retrospective study was approved by the local institutional review board (IRB). A waiver of consent was obtained from the IRB to access patient MRI data and other clinical records. Forty-six patients who underwent MRI examination for suspected prostate cancer were included. As part of this examination, routine clinical scans were performed and assessed in accordance with version 2 of the Prostate Imaging Reporting and Data System (PI-RADS v2) (3). Any lesions suspicious for prostate cancer were defined and reported on the clinical images by board-certified radiologists with sub-specialization in abdominopelvic imaging. Lesion contours were defined in DynaCAD (Philips, Best, Netherlands) and imported in the UroNav MRI/ultrasound guided fusion biopsy system (Philips, Best, Netherlands) for transrectal targeted biopsy. Systematic 12-core biopsy of the prostate was also performed in the same session as targeted biopsy, and the location of each tissue sample was recorded to enable correspondence between histology and imaging. The presence of prostate cancer in these tissue samples and the corresponding Gleason Grade groups were determined via routine clinical histopathologic analysis by board-certified pathologists.

This evaluation determined that 23 patients (age: 64±9 years; PSA: 9.5±7.5 ng/mL) had cancerous lesions in the prostate. Seventeen lesions were located (radiographically) in the peripheral zone of the prostate, 4 were located in the transition zone, and 2 extended into both the peripheral and transition zones. The PI-RADS v2 scores for these lesions ranged from 3 to 5, with 13 lesions scored as a 5, 8 lesions scored as a 4, and 2 lesions scored as a 3. Gleason Grade groups reported for the lesions ranged from 1 to 5, with 4 lesions scored as a 5, 1 lesion scored as a 4, 7 lesions scored as a 3, 8 lesions scored as a 2, and 3 lesions scored as a 1. A detailed summary of these clinical findings is presented in Table 1.

Biopsy results were cancer-negative from 21 patients. Two patients were not biopsied but had PI-RADS v2 lesion scores of 1 and 2 and were presumed cancer free, for a total of 23 patients without detectable cancer (age: 64±11 years; PSA: 12.2±23.8 ng/mL).

MRI data acquisition

All MR imaging was performed on a 3T clinical scanner (Discovery MR750; GE Healthcare, Waukesha, WI) using a 32-channel phased-array body coil surrounding the pelvis. Routine clinical scans were first acquired in accordance with PI-RADS v2 specifications (3). Axial DWI volumes (TR: 3900 ms, TE: 65 ms, matrix 160×160, FOV: 260 mm, slices: 30, slice thickness: 5 mm) were acquired at b-values of 50 and 1000 s/mm^2, and an ADC map was automatically generated from these DWI volumes by the scanner software. A LAVA-flex pulse sequence (20) was used to acquire axial T1-weighted water-only and fat-only pelvic volumes (TR: 4.12 ms, TE: 1.7 ms, flip angle: 12°, matrix: 320×224, FOV: 320 mm, slices: 104, slice thickness: 4 mm). Dynamic contrast-enhanced (DCE) MRI was performed using a time-resolved imaging of contrast kinetics (TRICKS) (21) protocol that acquired 32 frames with a temporal resolution of one frame every 7 seconds (TR: 4.6 ms, TE: 2.1 ms, flip angle: 30°, matrix: 256×168, FOV: 220 mm, slices: 32, slice thickness: 3 mm). Baseline-subtracted volumes were automatically generated from TRICKS data by the scanner software. These clinical datasets were retained as a reference to aid in the definition of tissue contours on RSI acquisitions, but were not otherwise evaluated as part of this study.

For RSI, an axially-oriented multi-shell DWI volume was acquired for each patient that sampled 5 b-values (0, 200, 1000, 2000, and 3000 s/mm^2) at 6 unique diffusion-encoding gradient directions (default tensor directions, one average per direction, δ: 25 ms, Δ: 37 ms, TR: 5000 ms, TE: 80 ms, resolution: 2.5×2.5 mm, matrix: 96×96 resampled to 128×128, slices: 34, slice thickness: 3 mm, fat saturation: spatial-spectral, parallel imaging: none, acquisition time: 5 min). The b = 0 s/mm^2 volumes were acquired using both forward and reverse phase encoding to allow for correction of distortion caused by B0 inhomogeneity (22). As an anatomical reference, a T2-weighted volume was acquired with scan coverage identical to that of the multi-shell DWI volume (TR: 6225 ms, TE: 100 ms, resolution: 0.75×0.75 mm, matrix: 320×320 resampled to 512×512, slices: 34, slice thickness: 3 mm, fat saturation: off, acquisition time: 5 min).

RSI MRI data post-processing

All post-processing and analysis of MRI data was performed using custom programs written in MATLAB (The MathWorks, Inc; Natick, MA). The multi-shell DWI volumes were first corrected for distortions due to B0 inhomogeneity, gradient nonlinearity, and eddy currents (12, 22). Because noise in MR images can bias estimated DWI parameters (18, 23), signal intensity in the multi-shell DWI volumes was corrected to account for the presence of the noise floor (18). Briefly, the mean background signal intensity of each volume was estimated and then subtracted from the observed signal intensity of each voxel to obtain the corrected signal intensity (S_{corr}). Isotropic diffusion in the prostate was assumed, so the 6 directional diffusion volumes at each b-value were averaged together. For comparison against RSI, conventional ADC maps were computed from this DWI data by fitting the signal at b-values 0 and 1000 s/mm^2 to a monoexponential signal decay model.

All tissue contouring was performed by a radiation oncologist (C.H.F.; 3 years of experience contouring images) and reviewed for accuracy by two board-certified radiologists (M.E.H.

and R.R.P.; 6 and 3 years of experience reviewing contours, respectively) using MIM software (MIM Software, Inc; Cleveland, OH). For patients without cancer, regions of interest (ROIs) were defined to include the entire prostate and seminal vesicles. To allow for examination of signal from different anatomical regions, separate sub-ROIs were also defined over the peripheral and transition zones of the prostate, as well as the seminal vesicles. For patients with prostate cancer, ROIs were defined over the tumor in agreement with standard-of-care clinical assessment: lesion signal intensity on all available imaging modalities (principally T2-weighted and DWI) was considered alongside pathologic findings to determine the extent of the tumor ROI. All ROIs were examined by the two radiologists and, if necessary, the contours were adjusted to achieve consensus between readers. The finalized ROIs were then exported as binary masks in a MATLAB-readable format.

Multicompartmental RSI modeling

The RSI model is defined by the following formula:

$$S_{corr}(b) = \sum_{i=1}^{K} C_i e^{-bD_i}$$

where $S_{corr}(b)$ denotes the noise-corrected DWI signal at a particular b-value, K is the number of tissue compartments, C_i is a unit-less weighting factor describing the contribution of a particular compartment to the overall signal, and D_i is the compartmental ADC. By convention, the compartments are ordered from lowest to highest ADC, such that the first compartment (C_1) describes the most restricted class of diffusion. To determine optimal K and D_i values for the prostate, a global fitting of the model to the multi-shell DWI data from all voxels within all ROIs (normal+cancer tissue; >200,000 voxels) was performed, with K ranging from 2 to 5 (the maximum number of compartments was limited to the number of b-values employed during image acquisition). For each K value, model fitting was performed using a simplex search method (24) to minimize a quadratic (convex) cost function that quantifies the difference between observed and model-predicted signal values for all voxels simultaneously. To compute the cost function for a given set of D_i values, a nonnegative least-squares optimization (25) was necessary to estimate the corresponding C_i values and generate the model-predicted signal values. Minimizing this cost function returned optimal D_i values for each of the K compartments of the model. Once optimal RSI models were determined, tissue signal-contribution (C_i) maps were computed for each patient via nonnegative least-squares fitting of the model to the signal-vs-b-value curve from each voxel. Computation time for these voxel-wise signal-contribution maps was 0.59 ± 0.01 s/patient on a desktop computer with 64 GB RAM and an 8-core, 2.40 GHz CPU (Intel Xeon E5–2630 v3).

Fractional signal contribution or “signal fraction” was computed from the signal contribution by normalizing the C value for each compartment by the sum of C values for all compartments in the model: $C_i / \sum_{i=1}^{K} C_i$. This normalization eliminates T2, proton density, and scanner-dependent scaling effects that limit comparisons across patients.

Statistical analysis

To assess the variance of the D_i parameters estimated from RSI model fitting, 1000 iterations of bootstrapping were performed by randomly resampling the DWI signal data at the patient level and re-fitting the RSI models to the resampled data. 95% confidence intervals for each D_i value were then computed from the bootstrapped parameter distributions.

To determine how well the various multi-compartmental RSI models described the prostate diffusion data, the Bayesian Information Criterion (BIC; (26)) was computed for each model as follows:

$$BIC = \ln(N) \cdot K + N \cdot \ln\left(\frac{R}{N}\right)$$

where N is the sample size (taken to be the number of patients in this study — 46), K is the number of tissue compartments in the model, and R is the model-fitting's sum of squared residuals. The relative BIC (ΔBIC) for each RSI model was calculated: $\Delta BIC = BIC_i - BIC_{min}$, where BIC_i is the BIC value of a particular model and BIC_{min} is the minimal BIC observed from any of the models.

Relative fitting residual (percent variance of the difference between model-predicted and measured signal) was recorded from 1000 bootstrap iterations of model-fitting with patient-level resampling to assess each model's goodness-of-fit. Paired t-tests (α=0.05) were used to determine if the fitting residuals from RSI models were smaller than those from conventional ADC mapping. For the optimal RSI model with lowest ΔBIC, one-way analysis of variance (ANOVA) was performed to check for any significant variation in fitting residual between anatomical regions of the prostate (peripheral and transition zones, seminal vesicles, and tumors). If significant variation between regions was detected, two-sample t-tests (α=0.05) were performed to ascertain which specific regions were significantly different. Compartmental signal fractions were compared between normal tissues (peripheral zone, transition zone, seminal vesicles) and tumors using two-sample t-tests (α=0.05).

To quantify tumor prominence on the conventional DWI images (ADC maps and trace DWI images at each b-value) and RSI C_1 maps, tumor contrast-to-noise ratio (CNR) and signal intensity ratio (SIR) were computed. CNR was calculated as the absolute difference in mean signal between the tumor and surrounding parenchyma, normalized by the standard deviation of the non-tumor signal. SIR was defined as the ratio of mean signal in the tumor to mean signal in the surrounding parenchyma, and has previously been used as a measure of tumor conspicuity (8). CNR and SIR were compared between the conventional DWI images and RSI C_1 maps using paired t-tests (α=0.05). CNR and SIR were also compared between the C_1 maps of RSI models with different numbers of compartments using paired t-tests (α=0.05). The hypothesis testing described above was all performed at the ROI-level (rather than the voxel level), meaning that voxel-wise estimates were averaged within each ROI prior to comparison.

Results

Optimal ADC values and 95% confidence intervals are listed in Table 2 for the different RSI models, alongside the relative BIC (ΔBIC) for each model. ΔBIC values were substantially lower for the 4- and 5-compartment models than for the 2- and 3-compartment models, with the 4-compartment model yielding the lowest BIC value overall. Figure 1 compares the bootstrapped distribution of fitting-residuals between conventional ADC mapping and the different RSI models. In normal prostate tissue, the fitting residuals from any of the RSI models was significantly lower than the residuals from conventional ADC mapping ($P < 0.05$). In tumor tissue, fitting residuals from the 3-, 4-, and 5-compartment RSI models were significantly lower than the residuals from conventional ADC mapping ($P < 0.05$). One-way ANOVA and subsequent pairwise t-tests indicated that fitting residuals from the 4-compartment model varied significantly between each of the different anatomical regions of the prostate ($P < 0.05$ for ANOVA and all pairwise t-tests). Mean fitting residual (in percent variance) was lowest in the peripheral zone (0.05 %), followed in ascending order by the mean residual in the transition zone (0.06 %), seminal vesicles (0.10 %), and tumors (0.11 %). Overall, an improved fit to the data (i.e., reduced fitting residual) was observed with increasing RSI model order. As model order increased from 2 to 5 compartments, the fitting residual decreased by 0.15 % across all voxels, 0.11 % in the peripheral zone, 0.11 % in the transition zone, 0.14 % in the seminal vesicles, and 4.57 % in tumors. Tumor tissue showed the largest reduction in fitting residual by increasing model order.

Signal contribution (C_i) maps that were computed from the optimized RSI models are shown in Figure 2 for a subject with a primary tumor in the transition zone. The compartmental signal fractions of different tissues are quantified in Figure 3. Across all models, prostate tumors showed a significantly greater ($P < 0.05$) proportion of signal from compartment C_1 than was observed in normal tissue. With the 4- and 5-compartment RSI models, the fraction of signal from C_2 was also significantly higher ($P < 0.05$) in tumors compared to normal tissue, while that of C_3 was significantly lower ($P < 0.05$). The signal fractions from both C_3 of the 3-compartment model and C_4 of the 4-compartment model were significantly lower in tumors than in any region of normal prostate tissue ($P < 0.05$ for both comparisons).

Among normal tissues, the peripheral zone and transition zone had substantially different signal-fraction profiles. For all models, the C_1 signal fraction was significantly greater ($P < 0.05$) in the transition zone than the peripheral zone. In the 2- and 3-compartment models, the C_2 signal fraction was significantly larger in the peripheral zone ($P < 0.05$). In the 4- and 5-compartment models, the C_2 signal fraction was significantly higher in the transition zone ($P < 0.05$). The 4-compartment model showed a significantly greater proportion of signal from C_3 in the peripheral zone ($P < 0.05$). The signal proportions computed from the 5-compartment model differed significantly between the peripheral and transition zones in compartments C_3 ($P < 0.05$) and C_4 ($P < 0.05$). In the 4^{th} compartment of the 4-compartment model and the 5^{th} compartment of the 5-compartment model (which have the highest D_i values and correspond to the vessel images in Figure 2) the signal fraction from the transition zone was significantly larger than from the peripheral zone ($P < 0.05$). None of the compartmental signal fractions were significantly different between the peripheral zone and seminal vesicles ($P > 0.1$ for all comparisons of all models).

Figure 4 compares tumor CNR and SIR from conventional DWI images to those from the C_1 maps of the optimized RSI models. CNR from RSI models with 3, 4, or 5 compartments was significantly higher than CNR from conventional ADC mapping ($P < 0.05$) or any of the trace DWI images ($P < 0.05$). CNR increased significantly when RSI model order increased from 2 to 3 compartments ($P < 0.05$), and from 3 to 4 compartments ($P < 0.05$). SIR from any of the RSI models was significantly greater than the SIR from the conventional ADC map ($P < 0.05$) or any of the trace images ($P < 0.05$). Tumor SIR on the RSI C_1 map generally increased with the number of model compartments. The increase in SIR from 2 to 3 compartments was statistically significant ($P < 0.05$), as was the increase in SIR from 3 to 4 compartments ($P < 0.05$).

Discussion

In this study, we evaluated different RSI models to determine an optimal characterization of diffusion properties in both normal and cancerous prostate tissue. The diffusion properties (D_i) of each model were determined through simultaneous, global fitting to diffusion-signal data from 46 clinically-representative patients (over 200,000 voxels). Unlike more conventional DWI analysis that examines only the averaged signal within pre-identified lesion ROIs (27–29), our approach considers the diffusion properties of every tissue voxel, whether it is cancerous or not, throughout the entire prostate and seminal vesicles. Other multi-shell DWI methods have examined diffusion at the voxel level (14, 15), but the RSI approach employing fixed, globally-optimal D_i values enables more stable estimates than can be achieved with fully-independent model fitting at each voxel. Enhanced estimation stability is particularly important when fitting higher-order multicompartmental models as was done in this study.

To examine how RSI fits into the broader context of prostate MRI, it is important to recognize that RSI and many other modeling approaches are all specific implementations of a broader multicompartmental framework. These implementations differ principally in the number of model compartments, whether the compartmental diffusion coefficients are free parameters or fixed, and whether the model describes the normalized or unnormalized DWI signal. The intravoxel incoherent motion (IVIM) model, for example, is a biexponential signal-decay model with two freely varying diffusion coefficients per signal curve: a slow component representing true diffusion in tissue and a fast pseudo-diffusion component that accounts for perfusion in the vascular network (30). By contrast, RSI does not explicitly prescribe a particular number of compartments (here we empirically determined that 4 compartments are appropriate for prostate imaging), and the compartmental diffusion coefficients are fixed across voxels. RSI and IVIM are also generally applied to study different aspects of physiology. IVIM aims to quantify fast-flowing (very high ADC) fluid in the vasculature and therefore requires sampling of the DWI signal at very low b-values (< 100 s/mm^2) (31), while RSI is primarily concerned with restricted diffusion (very low ADC) in tumors and as a result requires sampling at very high b-values (≥ 2000 s/mm^2) (12). The “Vascular, Extracellular, and Restricted Diffusion for Cytometry in Tumors” (VERDICT) framework models DWI signal similarly to RSI. It specifies a 3-compartment model that represents signal contributions from restricted diffusion within cells, hindered diffusion within the extracellular-extravascular space, and pseudo-diffusion (flow) within blood

vessels (14, 32). This *a priori* decomposition of the DWI signal turns out to be quite similar to that of the 3-compartment RSI model empirically determined in this study (D_1: 8.7e-4, D_2: 2.6e-3, D_3: 9.1e-3 mm^2/s). Although the diffusion coefficients of the VERDICT model compartments are allowed to vary freely, in practice they may be fixed as with RSI in order to enhance model-fitting stability (32). The precise mathematical forms of the VERDICT compartments may also vary from the RSI compartments outlined here, but they nonetheless seek to examine the same aspects of tissue microstructure. Techniques such as luminal water imaging (33) and Hybrid Multidimensional MRI (15) are significant departures from the RSI approach presented here because they acquire image data at multiple echo times in order to measure T2 within different tissue compartments. T2 effects can be readily incorporated into RSI through addition of an exponential decay term dependent on T2 and echo time, resulting in a model similar to that of Hybrid Multidimensional MRI (minus the histological interpretation of the different compartments (15)). Unfortunately, lacking data acquired at multiple echo times that are necessary to investigate T2, we must reserve any direct comparisons between these techniques and RSI for future work. DWI signal normalization is enforced by all of these models except RSI. Normalization allows for easier physiological interpretation of results by converting signal contributions, generally dependent on proton density and scanner-specific factors, into volume fractions related to the concentration of specific cells or vessels, depending on the model (15, 30, 32). However, signal normalization can produce visually noisy parameter maps that might limit the conspicuity of specific features like tumors. For this reason, RSI signal contribution maps, like those shown in this study, are generally left unnormalized to ensure high tumor visibility.

Compared to the monoexponential signal model widely used for conventional ADC mapping, the multicompartmental RSI models examined in this study showed substantially better fits (i.e., lower fitting residuals) to DWI data from the prostate. This aligns with the results of previous studies that suggest the standard monoexponential model does not adequately describe the diffusion characteristics of the prostate (15, 18, 32, 34, 35). While PI-RADS specifies careful application of this model only over the range of b-values where the DWI signal can be well-approximated by a monoexponential decay (~100–1000 s/mm^2) (3), synthetic DWI methods regularly use the monoexponential model to extrapolate DWI signal far beyond this range (36, 37). Given the poor fit of the monoexponential model to high-b-value DWI data in this study, it is likely that the standard monoexponential approach to synthetic DWI introduces significant error into the extrapolated signal data and may need to be reexamined.

Among the RSI models examined in this study, the lowest BIC was observed from the 4-compartment model. This suggests that it provides the optimal characterization of diffusion properties throughout the entire prostate and seminal vesicles. BIC is a more conservative metric (biased towards model parsimony) than the Akaike information criterion (AIC), which is also commonly used to compare different models. A conservative information criterion is an appropriate choice for this study since prevailing DWI models have relatively few tissue compartments compared to what we examined here. Even the more advanced approaches like VERDICT and Hybrid Multidimensional MRI are limited to only 3 compartments (14, 15). Overfitting was also a more likely pitfall for this study than underfitting, since models with 5 or fewer compartments were fit to hundreds of thousands

of voxels simultaneously, which reinforces the selection of a conservative information criterion like BIC (38).

By examining the optimal D_i values for the 4-compartment model, we can begin to discern the different types of diffusion that contribute to DWI signal in the prostate. The optimal D value of compartment C_1, 5.2e-4 mm^2/s, is consistent with the characterization of restricted diffusion from previous studies (12, 16–18). Compartment C_2 likely accounts for hindered diffusion through the extracellular extravascular space (12, 39), having an optimal D of 1.9e-3 mm^2/s. Compartment C_3, with an optimal D of 3.0e-3 mm^2/s, reflects the free diffusion of water (12, 40). Finally, the fourth compartment C_4 considers rapid pseudo-diffusion (IVIM flow effects (30)) with an optimal D much greater than that of free diffusion (>3.0e-2 mm^2/s). We were unable to estimate a precise D value for this pseudo-diffusion component because the smallest non-zero b-value used for data acquisition (200 s/mm^2) was much too high for reliable measurement of the rapidly-decaying signal from vascular flow. Precise estimation of this D value would require additional sampling of the DWI signal at b-values less than 100 s/mm^2 (31).

Similarly, when we report a D value of 0 s/mm^2, either as the point estimate for compartment 1 of the 5-compartment model or as the lower-bound of the 95% confidence interval for compartment 1 of the 3-, 4-, and 5-compartment models, we do not mean to assert that there is no diffusion at all. Rather, we are stating that diffusion in this compartment is too slow for us to measure given the relatively long diffusion time at which data were acquired. There is evidence this compartment with D of “0” accounts for diffusion of intracellular water (12, 41), but further investigation is needed to verify this directly. If this compartment does in fact correspond to intracellular diffusion, it could potentially be a more accurate measurement of restricted diffusion than estimates from previous studies using RSI (16–19) or VERDICT (32), which likely included contributions from highly-hindered or tortuous extracellular diffusion (42) in the reported “restricted diffusion” compartment.

By fitting an RSI model to multi-shell diffusion data from the prostate, the distribution of signal among the various tissue compartments is revealed. This distribution may provide insight into the cytostructural changes that accompany prostate cancer development. Of particular interest is the signal contribution from compartment 1, i.e., the compartment with lowest diffusion coefficient D. Previous RSI studies (16–19) have linked increased signal from this compartment to increased tissue cellularity, an important prognostic indicator for prostate cancer (19, 43). Here we showed that the signal contribution from compartment 1 was significantly higher in tumors than in normal prostatic tissue, in agreement with those previous findings. Recent work by Chatterjee *et al.* (15) suggests that diffusional changes accompanying prostate cancer result from an increase in epithelial cell partial volume, rather than a just simple increase in tissue cellularity. Increased signal contribution observed in compartment 1 of tumors may therefore be attributed to a cancer-induced proliferation of tightly packed epithelial cells, but thorough histological examination would be necessary to verify this hypothesis.

Whatever the biophysical interpretation, it is clear that signal from RSI compartment 1 is enriched in tumors and may be helpful in the discrimination of prostate cancer. Such potential is highlighted by the significant increase in tumor CNR and SIR on RSI C_1 maps compared to conventional DWI. Improvement in CNR and SIR with RSI is driven in part from the reduction of signal in the parenchyma surrounding the tumor, which may help to discriminate between cancerous and benign tissue in radiographically-complex regions like the transition zone. Benign factors like BPH often decrease ADC in the transition zone and make identification of transition-zone tumors on conventional ADC maps difficult. By contrast, C_1 maps of the 4- and 5-compartment RSI models show almost no signal from benign tissue in the transition zone. This suppression of benign signal is a clinically-relevant benefit that could potentially outweigh the increase in scan time required to obtain data at the additional b-values needed to implement these models. Furthermore, higher order (4- and 5-compartment) models provide increased resolution that reveals diffusion-signal heterogeneity within tumors that is not apparent with simpler models. Tumor signal contributions from different model compartments may reflect different histological aspects of cancer progression, but this requires further investigation.

Finally, it should be mentioned that the RSI model-optimization procedure outlined here can be readily applied to tissues other than the prostate. As a straightforward extension of this study, we optimized RSI models for all tissues included in the original imaging volume, not just the prostate and seminal vesicles (see Supplementary Material online). We hypothesize that such models will better characterize the diffusion of both normal and malignant tissue throughout the body, potentially leading to improved identification of cancer in tissues beyond just the prostate. Future work will focus on leveraging these models to develop automated cancer screening methods.

Limitations

The generalizability of our findings may be limited since data was obtained from a relatively small number of subjects at a single institution. However, the subjects that were included are largely representative of the broader clinical population, and there was sufficient statistical power for the reported hypothesis testing. Another limitation is that this study evaluated the different models only in terms of their ability to fit diffusion data (i.e., using BIC and fitting residual) and not their actual sensitivity and specificity for prostate tumors. While the higher-order models showed a better fit to the diffusion data, it is not clear whether they would outperform simpler models in terms of classifying tissue as cancerous or benign. Nevertheless, the results of this current study are still valuable for developing a comprehensive model of diffusion in the prostate. Subsequent studies will evaluate RSI models for prostate cancer screening specifically. Finally, stronger conclusions could be drawn regarding the microstructural components underpinning RSI signal compartments if we had more comprehensive tissue samples available for this study (ideally whole-mount prostate sections). However, such extensive histology was not necessary for this study since our primary aim was to broadly characterize diffusion in both normal and cancerous prostate tissue, not to investigate specific radiologic-pathologic correspondence.

Conclusion

A 4-compartment RSI model with compartmental D values of 5.2e-4, 1.9e-3, 3.0e-3, and >3.0e-2 mm^2/s provides a comprehensive characterization of the diffusion properties in both normal and cancerous prostate tissue. Compartmental signal-contributions revealed by this model may help to discriminate tumors from healthy prostatic tissue and assess the microstructural changes that accompany prostate cancer development.

Supplementary Material

Refer to Web version on PubMed Central for supplementary material.

Acknowledgments:

Grant Support:

USAMR DoD W81XWH-17-1-0618

NIH K08 NIBIB EB026503

Prostate Cancer Foundation

UC San Diego Center for Precision Radiation Medicine

References

1. Norberg M, Egevad L, Holmberg L, Sparén P, Norlén BJ, Busch C: The sextant protocol for ultrasound-guided core biopsies of the prostate underestimates the presence of cancer. Urology 1997; 50:562–566. [PubMed: 9338732]
2. Hu Y, Ahmed HU, Carter T, et al.: A biopsy simulation study to assess the accuracy of several transrectal ultrasonography (TRUS)-biopsy strategies compared with template prostate mapping biopsies in patients who have undergone radical prostatectomy. BJU Int 2012; 110:812–820. [PubMed: 22394583]
3. Weinreb JC, Barentsz JO, Choyke PL, et al.: PI-RADS Prostate Imaging – Reporting and Data System: 2015, Version 2. Eur Urol 2016; 69:16–40. [PubMed: 26427566]
4. Ahmed HU, El-Shater Bosaily A, Brown LC, et al.: Diagnostic accuracy of multi-parametric MRI and TRUS biopsy in prostate cancer (PROMIS): a paired validating confirmatory study. The Lancet 2017; 389:815–822.
5. Rouvière O, Puech P, Renard-Penna R, et al.: Use of prostate systematic and targeted biopsy on the basis of multiparametric MRI in biopsy-naive patients (MRI-FIRST): a prospective, multicentre, paired diagnostic study. Lancet Oncol 2019; 20:100–109. [PubMed: 30470502]
6. Moore CM, Giganti F, Albertsen P, et al.: Reporting Magnetic Resonance Imaging in Men on Active Surveillance for Prostate Cancer: The PRECISE Recommendations—A Report of a European School of Oncology Task Force. Eur Urol 2017; 71:648–655. [PubMed: 27349615]
7. Le Bihan D: Molecular diffusion nuclear magnetic resonance imaging. Magn Reson Q 1991; 7:1–30. [PubMed: 2043461]
8. White NS, McDonald CR, Farid N, Kuperman JM, Kesari S, Dale AM: Improved Conspicuity and Delineation of High-Grade Primary and Metastatic Brain Tumors Using “Restriction Spectrum Imaging”: Quantitative Comparison with High B-Value DWI and ADC. Am J Neuroradiol 2013; 34:958–964. [PubMed: 23139079]
9. Hoeks CMA, Barentsz JO, Hambrock T, et al.: Prostate Cancer: Multiparametric MR Imaging for Detection, Localization, and Staging. Radiology 2011; 261:46–66. [PubMed: 21931141]
10. Hoeks CMA, Vos EK, Bomers JGR, Barentsz JO, Hulsbergen-van de Kaa CA, Scheenen TW: Diffusion-Weighted Magnetic Resonance Imaging in the Prostate Transition Zone:

Histopathological Validation Using Magnetic Resonance–Guided Biopsy Specimens. Invest Radiol 2013; 48:693–701. [PubMed: 23614975]

11. Oto A, Kayhan A, Jiang Y, et al.: Prostate Cancer: Differentiation of Central Gland Cancer from Benign Prostatic Hyperplasia by Using Diffusion-weighted and Dynamic Contrast-enhanced MR Imaging. Radiology 2010; 257:715–723. [PubMed: 20843992]
12. White NS, McDonald CR, Farid N, et al.: Diffusion-Weighted Imaging in Cancer: Physical Foundations and Applications of Restriction Spectrum Imaging. Cancer Res 2014; 74:4638–4652. [PubMed: 25183788]
13. White NS, Leergaard TB, D'Arceuil H, Bjaalie JG, Dale AM: Probing Tissue Microstructure with Restriction Spectrum Imaging: Histological and Theoretical Validation. Hum Brain Mapp 2013; 34:327–346. [PubMed: 23169482]
14. Panagiotaki E, Walker-Samuel S, Siow B, et al.: Noninvasive Quantification of Solid Tumor Microstructure Using VERDICT MRI. Cancer Res 2014; 74:1902–1912. [PubMed: 24491802]
15. Chatterjee A, Bourne RM, Wang S, et al.: Diagnosis of Prostate Cancer with Noninvasive Estimation of Prostate Tissue Composition by Using Hybrid Multidimensional MR Imaging: A Feasibility Study. Radiology 2018; 287:864–873. [PubMed: 29393821]
16. Rakow-Penner RA, White NS, Parsons JK, et al.: Novel technique for characterizing prostate cancer utilizing MRI restriction spectrum imaging: proof of principle and initial clinical experience with extraprostatic extension. Prostate Cancer Prostatic Dis 2015; 18:81–85. [PubMed: 25559097]
17. McCammack KC, Schenker-Ahmed NM, White NS, et al.: Restriction spectrum imaging improves MRI-based prostate cancer detection. Abdom Radiol 2016; 41:946–953.
18. Karunamuni RA, Kuperman J, Seibert TM, et al.: Relationship between kurtosis and biexponential characterization of high b-value diffusion-weighted imaging: application to prostate cancer. Acta Radiol 2018; 59:1523–1529. [PubMed: 29665707]
19. Liss MA, White NS, Parsons JK, et al.: MRI-Derived Restriction Spectrum Imaging Cellularity Index is Associated with High Grade Prostate Cancer on Radical Prostatectomy Specimens. Front Oncol 2015; 5.
20. Li XH, Zhu J, Zhang XM, et al.: Abdominal MRI at 3.0 T: LAVA-flex compared with conventional fat suppression T1-weighted images. J Magn Reson Imaging 2014; 40:58–66. [PubMed: 24222639]
21. Korosec FR, Frayne R, Grist TM, Mistretta CA: Time-resolved contrast-enhanced 3D MR angiography. Magn Reson Med 1996; 36:345–351. [PubMed: 8875403]
22. Holland D, Kuperman JM, Dale AM: Efficient correction of inhomogeneous static magnetic field-induced distortion in Echo Planar Imaging. NeuroImage 2010; 50:175–183. [PubMed: 19944768]
23. Taylor PA, Biswal B: Geometric analysis of the b-dependent effects of Rician signal noise on DTI estimates and determining an optimal b-value. Magn Reson Imaging 2011; 29:777–788. [PubMed: 21550747]
24. Lagarias JC, Reeds JA, Wright MH, Wright PE: Convergence Properties of the Nelder--Mead Simplex Method in Low Dimensions. SIAM J Optim 1998; 9:112–147.
25. Lawson CL, Hanson RJ: Solving Least-Squares Problems. Upper Saddle River, NJ: Prentice Hall; 1974:161.
26. Schwarz G: Estimating the Dimension of a Model. Ann Stat 1978; 6:461–464.
27. Vidić I, Egnell L, Jerome NP, et al.: Modeling the diffusion-weighted imaging signal for breast lesions in the b = 200 to 3000 s/mm2 range: quality of fit and classification accuracy for different representations. Magn Reson Med 2020; 00:1–13.
28. Donati OF, Mazaheri Y, Afaq A, et al.: Prostate Cancer Aggressiveness: Assessment with Whole-Lesion Histogram Analysis of the Apparent Diffusion Coefficient. Radiology 2013; 271:143–152. [PubMed: 24475824]
29. Vargas HA, Akin O, Franiel T, et al.: Diffusion-weighted Endorectal MR Imaging at 3 T for Prostate Cancer: Tumor Detection and Assessment of Aggressiveness. Radiology 2011; 259:775–784. [PubMed: 21436085]

30. Le Bihan D, Breton E, Lallemand D, Aubin ML, Vignaud J, Laval-Jeantet M: Separation of diffusion and perfusion in intravoxel incoherent motion MR imaging. Radiology 1988; 168:497–505. [PubMed: 3393671]

31. Döpfert J, Lemke A, Weidner A, Schad LR: Investigation of prostate cancer using diffusion-weighted intravoxel incoherent motion imaging. Magn Reson Imaging 2011; 29:1053–1058. [PubMed: 21855241]

32. Panagiotaki E, Chan RW, Dikaios N, et al.: Microstructural Characterization of Normal and Malignant Human Prostate Tissue With Vascular, Extracellular, and Restricted Diffusion for Cytometry in Tumours Magnetic Resonance Imaging. Invest Radiol 2015; 50:218. [PubMed: 25426656]

33. Hectors SJ, Said D, Gnerre J, Tewari A, Taouli B: Luminal Water Imaging: Comparison With Diffusion-Weighted Imaging (DWI) and PI-RADS for Characterization of Prostate Cancer Aggressiveness. J Magn Reson Imaging 2020; 52:271–279. [PubMed: 31961049]

34. Quentin M, Pentang G, Schimmöller L, et al.: Feasibility of diffusional kurtosis tensor imaging in prostate MRI for the assessment of prostate cancer: Preliminary results. Magn Reson Imaging 2014; 32:880–885. [PubMed: 24848289]

35. Wang X, Tu N, Qin T, Xing F, Wang P, Wu G: Diffusion Kurtosis Imaging Combined With DWI at 3-T MRI for Detection and Assessment of Aggressiveness of Prostate Cancer. Am J Roentgenol 2018; 211:797–804. [PubMed: 30085835]

36. Cui Y, Han S, Liu M, et al.: Diagnosis and Grading of Prostate Cancer by Relaxation Maps From Synthetic MRI. J Magn Reson Imaging 2020; 52:552–564. [PubMed: 32027071]

37. Arita Y, Takahara T, Yoshida S, et al.: Quantitative Assessment of Bone Metastasis in Prostate Cancer Using Synthetic Magnetic Resonance Imaging. Invest Radiol 2019; 54:638–644. [PubMed: 31192827]

38. Dziak JJ, Coffman DL, Lanza ST, Li R, Jermiin LS: Sensitivity and specificity of information criteria. Brief Bioinform 2020; 21:553–565. [PubMed: 30895308]

39. Koh TS, Bisdas S, Koh DM, Thng CH: Fundamentals of tracer kinetics for dynamic contrast-enhanced MRI. J Magn Reson Imaging 2011; 34:1262–1276. [PubMed: 21972053]

40. Le Bihan D: Looking into the functional architecture of the brain with diffusion MRI. Nat Rev Neurosci 2003; 4:469–480. [PubMed: 12778119]

41. Hope TR, White NS, Kuperman J, et al.: Demonstration of Non-Gaussian Restricted Diffusion in Tumor Cells Using Diffusion Time-Dependent Diffusion-Weighted Magnetic Resonance Imaging Contrast. Front Oncol 2016; 6.

42. White NS, Dale AM: Distinct effects of nuclear volume fraction and cell diameter on high b-value diffusion MRI contrast in tumors. Magn Reson Med 2014; 72:1435–1443. [PubMed: 24357182]

43. Kuwano H, Miyazaki T, Tsutsumi S, et al.: Cell Density Modulates the Metastatic Aggressiveness of a Mouse Colon Cancer Cell Line, Colon 26. Oncology 2004; 67:441–449. [PubMed: 15714001]

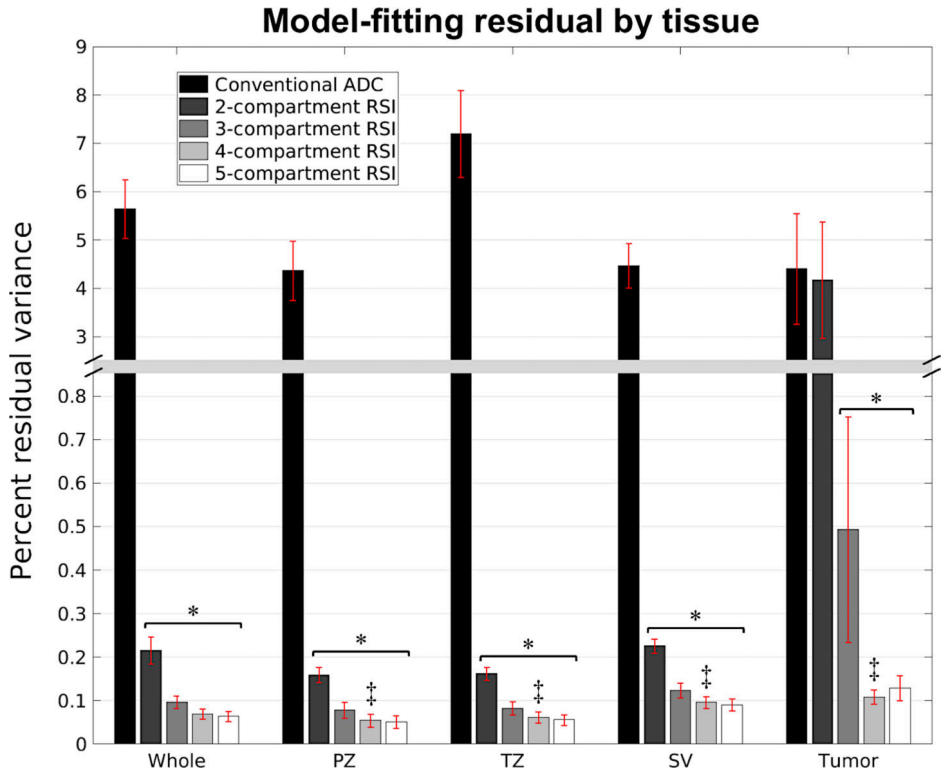

Figure 1:

RSI model-fitting residual by tissue type. Each bar shows the mean and standard deviation of 1000 bootstrap estimates of the fitting residual for a particular model and tissue type. A significant decrease in fitting residual compared to conventional ADC mapping is indicated by an asterisk (*). Double daggers (‡) denotes a significant difference in fitting residual from the 4-compartment model (the model with lowest ΔBIC) between the different anatomical regions of the prostate. Whole: whole prostate plus seminal vesicles, PZ: peripheral zone of the prostate, TZ: transition zone of the prostate, SV: seminal vesicles.

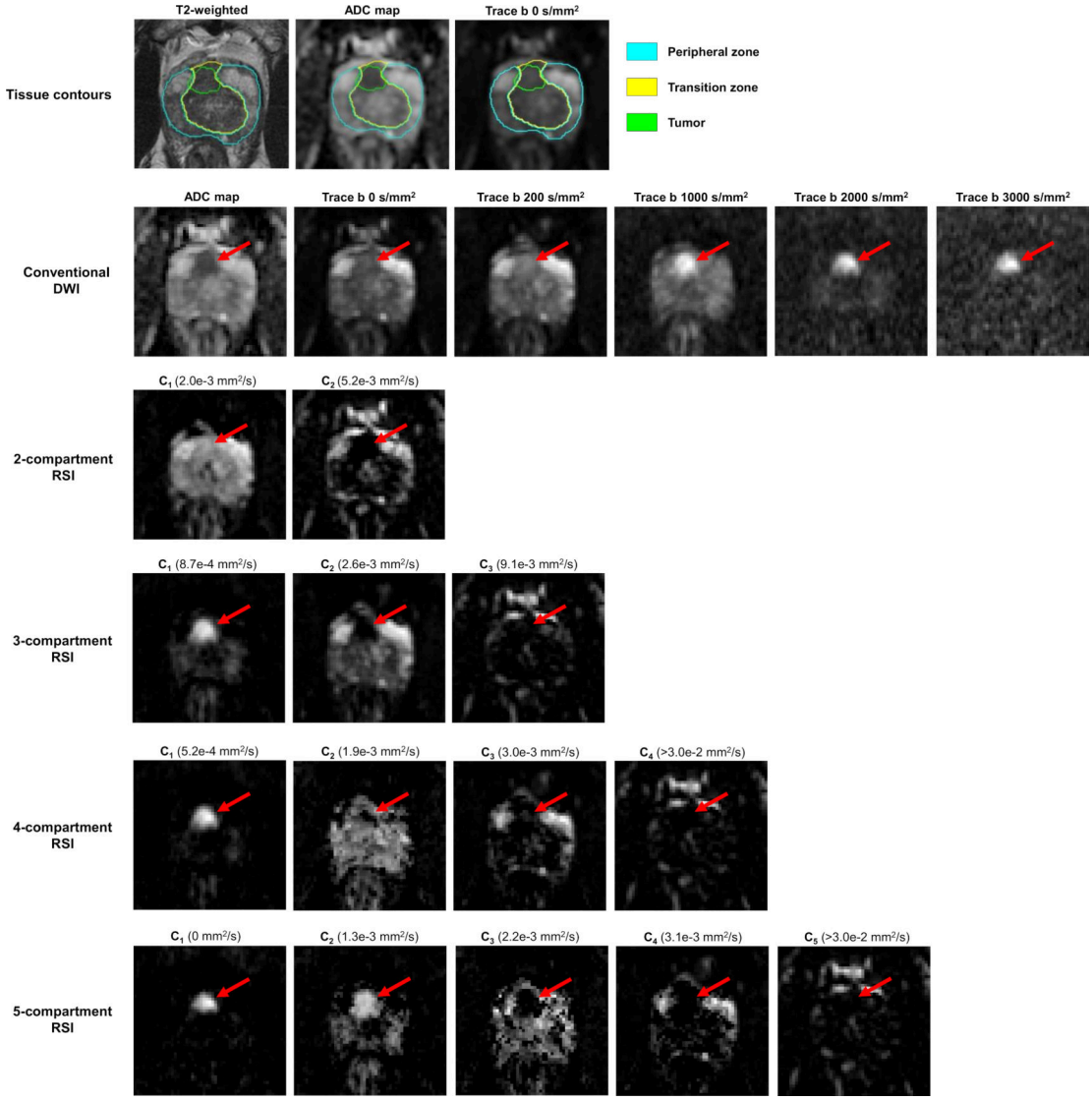

Figure 2:

Axial images of the prostate from a patient with a primary tumor (red arrow) in the transition zone (PI-RADS v2 score: 5, Gleason Grade group: 2). The top row details tissue contours defined on the axial slice shown here, overlaid on both a high-resolution T2-weighted image and lower-resolution DWI images. Conventional DWI images are shown in the second row, with RSI signal-contribution maps (C_i) calculated from the optimized models in the following rows. The corresponding D_i of each compartment is listed in parentheses next to the compartment label. The tumor appears as a bright region of the C_1 map of each model. Note the reduction of signal in surrounding parenchyma as model order increases, particularly of benign signal in the transition zone. The 4- and 5-compartment RSI models show tumor signal contributions from multiple compartments, revealing diffusion-signal heterogeneity within the tumor that is not apparent in the conventional ADC map.

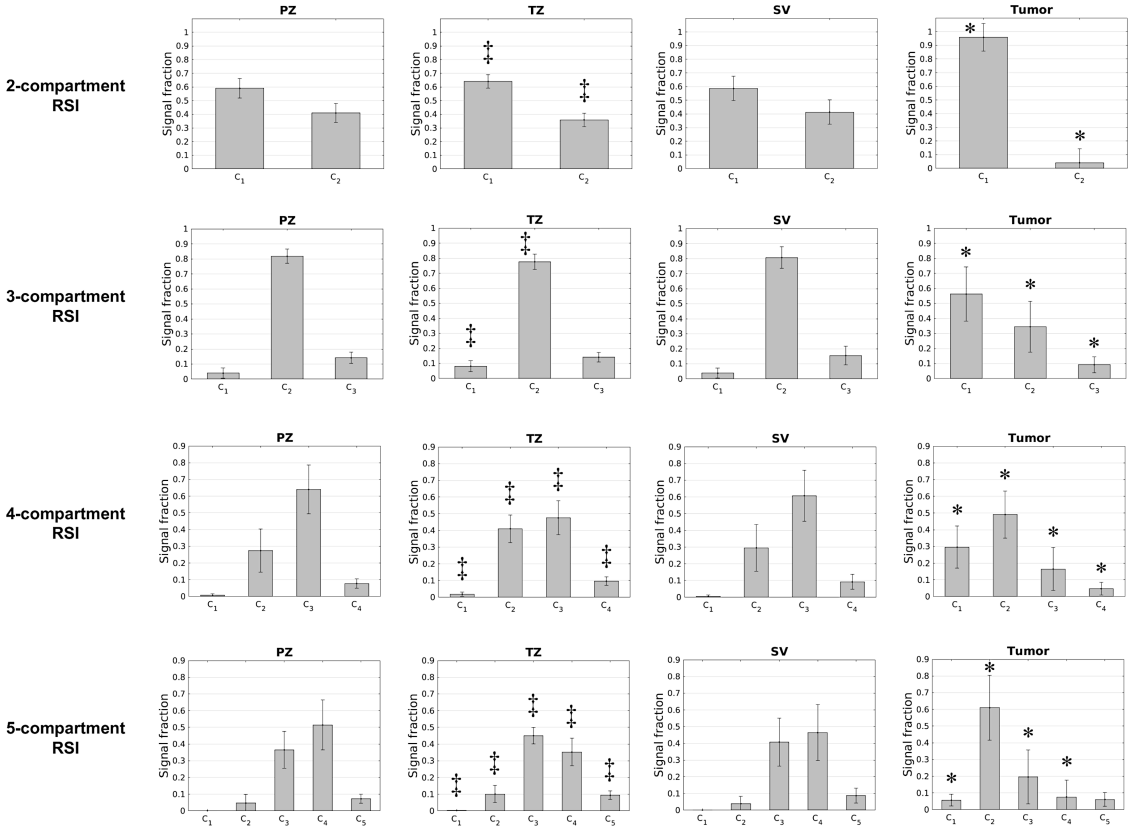

Figure 3:

Compartmental signal fractions of different tissues for each RSI model. The height of each bar indicates the mean signal fraction across all subjects, with the overlaid error bar indicating the standard deviation. An asterisk (*) over a bar indicates that the signal fraction in this compartment is significantly different in tumors compared to normal tissue (peripheral zone, transition zone, or seminal vesicles). Double daggers (‡) indicate a significant difference in signal fraction between the transition and peripheral zones. Signal fractions were not significantly different between the peripheral zone and seminal vesicles. PZ: peripheral zone of the prostate, TZ: transition zone of the prostate, SV: seminal vesicles.

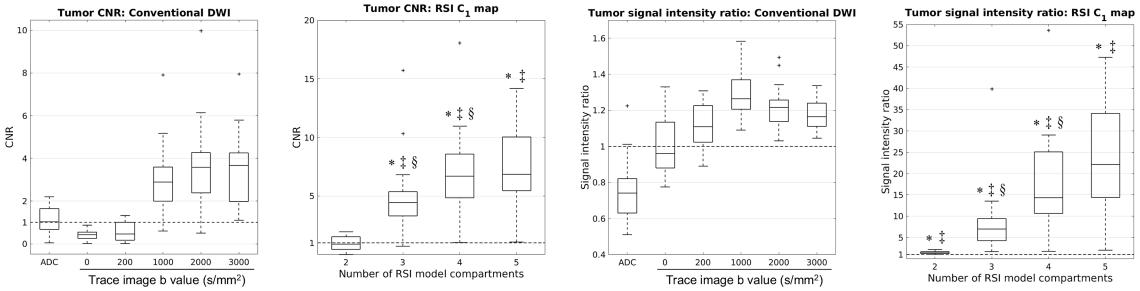

Figure 4:

Tumor contrast to noise ratio (CNR) and signal intensity ratio (SIR) on conventional DWI images and C_1 maps of optimized RSI models. The dashed horizontal line marks the 1:1 tumor:parenchyma CNR or SIR. The upper and lower bounds of each box indicate the interquartile range of CNRs/SIRs from all patients with tumors, while the horizontal line within each box denotes the median CNR/SIR. The whiskers mark the minimum and maximum CNRs/SIRs, excluding any outliers which are marked by a "+". An asterisk (*) indicates that tumor CNR/SIR is significantly higher on RSI C_1 maps than conventional ADC maps. Double daggers (‡) denotes a significant increase in CNR/SIR compared to the trace DWI images at any b-value. A section mark (§) indicates a significant increase in tumor CNR/SIR compared to the RSI model with one fewer compartment.

Table 1:

Clinical findings from the 23 patients with prostate lesions included in this study.

Subject	Age	PI-RADS v2 lesion score	Radiologic lesion location	PSA (ng/mL)	Gleason Grade Group	Pathology Specimen Type	Clinical Risk Group
1	59	5	Right TZ and PZ	7.8	2	Biopsy (Systematic)	FIR
2	54	5	Right PZ	10.6	3	Biopsy (Systematic), Radical Prostatectomy	UIR
3	71	5	Right PZ and TZ	4.0	5	Biopsy (Systematic and Targeted), Radical Prostatectomy	HR
4	72	5	Right PZ	5.7	2	Biopsy (Systematic)	UIR
5	54	5	Right PZ	7.3	3	Biopsy (Systematic), Radical Prostatectomy	HR
6	63	5	Right PZ	16.8	3	Biopsy (Systematic), Radical Prostatectomy	HR
7	74	5	Right PZ	29.3	5	Biopsy (Systematic)	HR
8	53	4	Left PZ	8.0	1	Biopsy (Systematic), Radical Prostatectomy	FIR
9	66	4	Right PZ	8.7	3	Biopsy (Systematic and Targeted)	UIR
10	67	5	Left PZ	4.6	2	Biopsy (Systematic and Targeted)	FIR
11	62	5	Left PZ	14.0	3	Biopsy (Systematic), Radical Prostatectomy	HR
12	74	4	Left PZ	4.4	3	Biopsy (Systematic and Targeted), Radical Prostatectomy	UIR
13	50	3	Left PZ	4.3	2	Biopsy (Systematic), Radical Prostatectomy	HR
14	65	4	Right TZ	8.0	1	Biopsy (Systematic)	LR
15	81	5	Anterior TZ	8.5	2	Biopsy (Systematic and Targeted)	FIR
16	77	5	Right PZ	3.5	4	Biopsy (Systematic), Radical Prostatectomy	HR
17	70	4	Left PZ	7.4	2	Biopsy (Systematic and Targeted)	FIR
18	58	4	Left PZ	7.4	2	Biopsy (Systematic), Radical Prostatectomy	UIR
19	62	4	Left PZ	5.0	1	Biopsy (Systematic)	LR
20	68	4	Right PZ	5.9	5	Biopsy (Systematic and Targeted), Radical Prostatectomy	HR
21	64	5	Midline to Right TZ	8.6	2	Biopsy (Systematic and Targeted)	FIR
22	51	5	Diffuse PZ	33.0	5	Biopsy (Systematic)	VHR
23	51	3	Right TZ	5.4	3	Biopsy (Systematic), Radical Prostatectomy	UIR

PI-RADS v2: Prostate Imaging – Reporting and Data System, version 2; PZ: peripheral zone of the prostate; TZ: transition zone of the prostate; PSA: prostate-specific antigen; FIR: Favorable intermediate risk; UIR: Unfavorable intermediate risk; HR: High risk; VHR: Very high risk.

Table 2:

Optimal compartmental apparent diffusion coefficient (D_i) values for RSI models of the prostate. The 95% confidence interval for each D_i value is shown in brackets. The relative Bayesian information criterion (ΔBIC) describes how well each model fits the data, with a lower ΔBIC indicating a better fit.

Number of tissue compartments	Optimal D_i for each compartment (mm^2/s)					ΔBIC
	1	2	3	4	5	
2	**2.0e-3** [1.6e-3, 2.3e-3]	**5.2e-3** [3.9e-3, >3e-2]				45.2
3	**8.7e-4** [0, 1.3e-3]	**2.6e-3** [2.3e-3, 2.7e-3]	**9.1e-3** [6.8e-3, 1e-2]			11.8
4	**5.2e-4** [0, 8e-4]	**1.9e-3** [1.6e-3, 2.0e-3]	**3.0e-3** [2.8e-3, 3.0e-3]	**3.0e-2** [1.2e-2, 3.0e-2]		0.0
5	**0** [0, 5.9e-4]	**1.3e-3** [1.2e-3, 1.7e-3]	**2.2e-3** [2.2e-3, 2.4e-3]	**3.1e-3** [3.1e-3, 3.3e-3]	**3.0e-2** [3.0e-2, 3.0e-2]	0.6

D_i: compartmental apparent diffusion coefficient.